

CHANDRA AND XMM OBSERVATIONS OF THE COMPOSITE SUPERNOVA REMNANT G327.1-1.1

TEA TEMIM^{1,2}, PATRICK SLANE¹, B. M. GAENSLER³, JOHN P. HUGHES⁴, ERIC VAN DER SWALUW⁵*Accepted to The Astrophysical Journal*

ABSTRACT

We present new X-ray imaging and spectroscopy of a composite supernova remnant G327.1-1.1 using the Chandra and XMM-Newton X-ray observatories. G327.1-1.1 has an unusual morphology consisting of a symmetric radio shell and an off center nonthermal component that indicates the presence of a pulsar wind nebula (PWN). Radio observations show a narrow finger of emission extending from the PWN structure towards the northwest. X-ray studies with ASCA, ROSAT, and BeppoSAX revealed elongated extended emission and a compact source at the tip of the finger that may be coincident with the actual pulsar. The high resolution Chandra observations provide new insight into the structure of the inner region of the remnant. The images show a compact source embedded in a cometary structure, from which a trail of X-ray emission extends in the southeast direction. The Chandra images also reveal two prong-like structures that appear to originate from the vicinity of the compact source and extend into a large bubble that is oriented in the north-west direction, opposite from the bright radio PWN. The emission from the entire radio shell is detected in the XMM data and can be characterized by a thermal plasma model with a temperature of ~ 0.3 keV, which we use to estimate the physical properties of the remnant. The peculiar morphology of G327.1-1.1 may be explained by the emission from a moving pulsar and a relic PWN that has been disrupted by the reverse shock.

Subject headings:

1. INTRODUCTION

Composite supernova remnants (SNRs) are those for which we see distinct evidence of the two fundamental components that characterize the aftermath of massive star collapse. The blast wave from the explosion sweeps up ISM material and heats it to X-ray emitting temperatures while accelerating electrons that produce radio synchrotron radiation in the compressed magnetic field. The highly magnetic, rapidly rotating neutron star (NS) that is left behind produces a particle wind which sustains an extended broadband synchrotron nebula of magnetic flux and relativistic particles. X-ray observations provide the thermal characteristics of the shell which allow us to constrain the explosion energy, age, and the surrounding ISM density. Simultaneously, the spectral and spatial properties of a pulsar wind nebula (PWN) allow us to infer the properties of the nebular pressure and magnetic field, and provide constraints on the central pulsar created in the explosion.

G327.1-1.1 is a composite SNR that was originally discovered as non-thermal radio source by Clark et al. (1973, 1975). It contains a bright central PWN whose structure is complex in both radio and X-ray bands. The radio morphology (Whiteoak & Green 1996) shows a faint shell, 17 arcmin in diameter, surrounding a bright non-thermal PWN component that is presumably powered by a yet-to-be-discovered pulsar. The bright part of the PWN is located off-center with respect to the SNR shell. A distinct finger-like structure protrudes from

the PWN in the northeast direction, possibly suggesting a picture in which a fast-moving pulsar is moving through the SNR, leaving the PWN in its wake. This type of PWN morphology indicated that the reverse shock of the SNR has disrupted the PWN (Blondin et al. 2001; van der Swaluw et al. 2004). The X-ray emission from G327.1-1.1 was first detected by Lamb & Markert (1981), who noticed an offset between the peak radio and X-ray emission. The composite nature of G327.1-1.1 was further confirmed by recent X-ray studies, which provide evidence of a compact X-ray source that is the likely counterpart for the pulsar powering the PWN emission (Slane et al. 1998; Sun et al. 1999).

There has also been evidence for thermal X-ray emission in G327.1-1.1 in previous studies, but the properties of this component are not well determined. ROSAT PSPC observations by Seward et al. (1996) reveal X-ray emission concentrated at the position of the PWN with some very faint emission extending outward toward the SNR shell. Using a simple blast-wave interpretation, they conclude that the remnant age is 7000 yr, although this value relies strongly on the inferred temperature of the outer emission component which is not well determined from the ROSAT data. ASCA observations also provide weak evidence for thermal emission (Sun et al. 1999) with $kT \sim 0.4$ keV. Using a Sedov model, their results imply a remnant age of 11000 yr, a preshock density of $n_0 = 0.1 \text{ cm}^{-3}$, and a swept-up mass of $50 M_\odot$. BeppoSAX observations indicate a temperature of about 0.2 keV, however (Bochinno & Bandiera 2003), which leads to an age of 29000 yr, $n_0 \sim 0.4 \text{ cm}^{-3}$, and a swept-up mass of $800 M_\odot$.

In this paper, we present *Chandra* and *XMM* X-Ray imaging and spectroscopy of G327.1-1.1, along with the Molonglo Observatory Synthesis Telescope (MOST) 843 MHz observations (Whiteoak & Green 1996) for compar-

¹ Harvard-Smithsonian Center for Astrophysics, CfA² Department of Astronomy, School of Physics and Astronomy, University of Minnesota³ Institute of Astronomy, School of Physics, The University of Sydney, NSW 2006, Australia⁴ Rutgers University⁵ Royal Netherlands Meteorological Institute (KNMI), The Netherlands

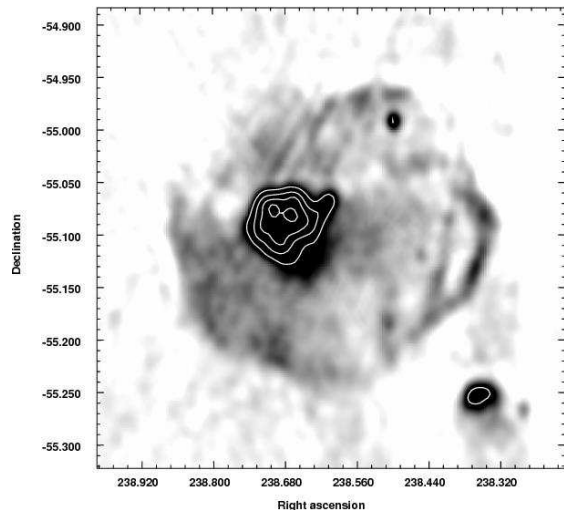


FIG. 1.— MOST 843 MHz radio image of G327.1-1.1 with a resolution of $43''$ and the PWN region contours overlaid, with levels of 0.05, 0.09, 0.13, and 0.21 Jy/beam Whiteoak & Green (1996). The image shows a faint shell, 17 arcmin in diameter, surrounding a bright non-thermal component, from which a narrow finger of emission extends to the northwest.

ison. Observations and data reduction are described in Section 2 and imaging and spectral analysis in Section 3. Section 4 discusses the nature of the thermal and non-thermal emission, remnant and PWN properties and morphology, and the evolutionary phase of G327.1-1.1. The conclusions are summarized in Section 5.

2. OBSERVATIONS AND DATA REDUCTION

G327.1-1.1 was observed with the Advanced CCD Imaging Spectrometer, ACIS-I, on board the *Chandra* X-ray observatory on 2001, July 15, under the observation ID 1955 and a total exposure time of 50 kiloseconds. The standard data reduction and cleaning were performed in Ciao Version 3.4. The XMM-Newton observations were carried out on 2004, Feb 07 with the MOS1, MOS2, and PN cameras for a total exposure time of 100 ks, under the observation ID 0203820101. The MOS cameras were operated in the Full Frame Mode with a “medium” filter setting, and the PN camera was operated in the Small Window Mode. The standard reduction of the data was performed using the XMM-SAS software, version 7.1.0, and resulted in a final exposure time of 85 ks for each of the MOS detectors, and 82 ks for the PN detector.

2.1. Imaging

In order to analyze the X-ray morphology of G327.1-1.1, images in various energy bands were created from the *Chandra* data. Point sources in the field were subtracted from the cleaned event file using the Ciao task *dmfilth*. The missing pixel values for each point source region were replaced by a Poisson distribution whose mean was determined from the pixel values of the background region surrounding each point source. X-ray images and the corresponding exposure maps, were created with a binning factor of 8 and convolved with a Gaussian function with $\sigma = 3$ pixels. Finally, the binned and smoothed images were divided by the exposure maps in order to correct for the differences in the spectral response and effective area across the field.

Images in multiple X-ray energy bands were also cre-

ated from the cleaned XMM-Newton MOS1 and MOS2 event files. Events from the regions that correspond to bright point sources in the field were removed from the data and were not refilled in this case. The images and the exposure maps in the corresponding energy bands were created using the SAS (version 7.1.0) software, with the spatial binning size set to $5''$. Since the background in the XMM images includes a non-vignetted component from the internal background and X-ray fluorescence, dividing by the exposure map tends to leave a hollow ring in the images. In order to remove the non-vignetted background component, we used the Filter Wheel Closed (FWC) data provided by the XMM-Newton EPIC Background Working Group at the University of Birmingham (<http://www.sr.bham.ac.uk/xmm3/BGproducts.html>), which are dominated by the internal instrumental background. FWC images of the internal background were created and subtracted from our data, after correcting for the difference in exposure times. Before subtracting the background and dividing by the exposure maps, all the images were smoothed by a Gaussian function with a width of 3 pixels ($15''$). Finally, the MOS1 and MOS2 images were combined using the SAS task *emosaic* to produce one final MOS image.

2.2. Spectroscopy

XMM-Newton MOS spectra were extracted from the cleaned and point source subtracted event files using the SAS (version 7.1.0) *especget* task, which generates spectra and the corresponding effective area and spectral response files. The spectra were extracted from a circular aperture with a radius of $5.2'$, centered on the PWN region of G327.1-1.1, and an annulus with an inner radius of $5.2'$ and an outer radius of $11.6'$ that mostly includes emission from the thermal shell. These regions are shown in Figure 4. Since there was no suitable region available for background extraction due to the spatial extent of the source, we used the combination of blank sky background and FWC data to estimate the background. The blank sky background event files were produced by the XMM-Newton EPIC Background Working Group at the University of Birmingham, using observations for many sky positions (Carter & Read 2007). The XMM Newton *Skycast* script was used to project the blank sky and FWC event files into sky coordinates and match it to our dataset. Spectra were then extracted from the same regions as the source spectra and corrected to the same exposure times. The blank sky background data is a combination of the sky background and the internal instrumental background, which can vary as a function of time. In order to determine the possible difference in the internal background levels between our observations and the background datasets, which were taken on different dates, we measured and compared the high energy (10–12 keV) fluxes at the positions of the detector that were out of the field of view. The blank sky high energy flux was found to be lower by 5% and 3% for the MOS1 and MOS2 observations, respectively. The spectra extracted from the FWC data were then multiplied by these factors and added to the blank sky spectra in order to account for the different levels in the internal background and produce a final background spectrum. The final backgrounds were then subtracted from the source spectra and grouped to include a minimum of 100 and 50 counts

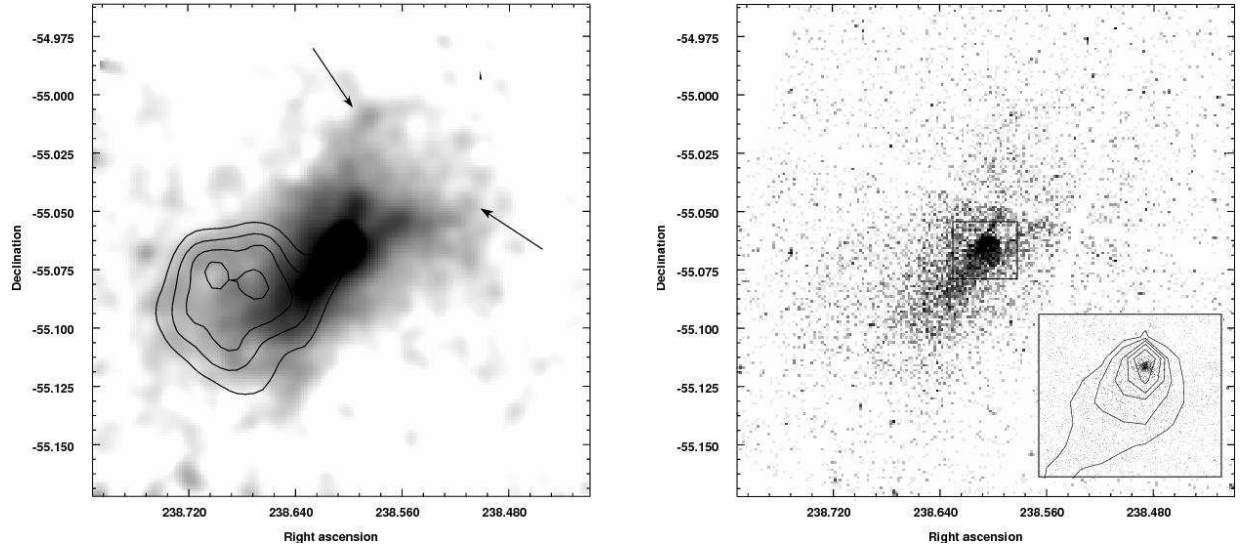


FIG. 2.— The left panel is the exposure corrected and smoothed *Chandra* ACIS image of G327.1-1.1 in the 0.5-10.0 keV band, with the contours of the radio image in Figure 1 overlaid. The image reveals a compact source at the tip of the radio finger, from which a trail of X-ray emission extends towards the southeast. A pair of bright prong-like structures originates from the vicinity of the compact source and extends into a large bubble-like structure, indicated by the arrows. The left panel shows the same image, binned by a factor of 8, but unsmoothed. The compact source region in the black box, approximately 1/5 by 1/5 in size, is zoomed in at the bottom right corner of the image. The image of the zoomed in region is unbinned and unsmoothed. The contours are the binned and smoothed contours from the same data.

TABLE 1
XMM SPECTRAL FITTING RESULTS

PARAMETER	PWN	Shell
$N_H(10^{22} \text{cm}^{-2})$	1.91 ± 0.07	(1.91)
Photon Index	2.11 ± 0.03	...
kT (keV)	0.29 ± 0.01	0.30 ± 0.01
Residual background temperature (keV)	(3.3)	3.3 ± 0.4
$F_X(\text{total observed})(\text{erg}/\text{cm}^2/\text{s})$	7.3E-12	4.0E-12
$F_X(\text{unabsorbed non-thermal})(\text{erg}/\text{cm}^2/\text{s})$	1.7E-11	...
$F_X(\text{unabsorbed thermal})(\text{erg}/\text{cm}^2/\text{s})$	9.8E-11	2.1E-10
$F_X(\text{unabsorbed background})(\text{erg}/\text{cm}^2/\text{s})$	1.3E-12	5.1E-12
Reduced χ^2 Statistic	1.08	1.26

NOTE. — The listed uncertainties are 1.6 sigma (90 % confidence) statistical uncertainties only. The apertures used in the spectral extractions are shown in Figure 4, and the spectra and fits are shown in Figure 5. The values in parantheses were held fixed. The fluxes were calculated in the 0.3-9.0 keV band and represent the average of the MOS1 and MOS2 flux values.

per bin for the PWN and the shell emission spectrum, respectively.

The *Chandra* ACIS spectra and the corresponding effective area and spectral response files were produced using the *specextract* script in *Ciao* version 3.4. The spectra were extracted from elliptical apertures shown in Figure 3, with each larger aperture excluding the counts from the inner apertures. Since the emission from the remnant covered the majority of the ACIS detector, corresponding background spectra from the same regions were extracted from the ACIS blank sky background files (<http://cxc.harvard.edu/ciao/threads/acisbackground/>). The blank sky data are produced from observations at various sky positions with high Galactic latitude and have been reprojected to the same sky coordinates as the source event file using the *aspect* solution for our observation. The background was subtracted and the resulting source spectra were grouped to include 30

counts in each bin for the two smaller apertures and 50 counts in each bin for the two larger apertures. Since G327.1-1.1 is located near the Galactic plane, the blank sky spectra most likely underestimate the background at lower energies, which may result in a residual Galactic background component.

3. ANALYSIS

3.1. X-ray Morphology

The *Chandra* ACIS raw and smoothed and exposure-corrected X-ray images of G327.1-1.1 in the 0.3-10.0 keV band are shown in Figure 2. The MOST radio image is shown in Figure 1 for comparison. The radio image shows a symmetric radio shell, 17 arcminutes in diameter, and a bright, off-center non-thermal component from which a narrow finger of emission extends in the north-west direction. The *Chandra* images show a compact source at the tip of this finger and more diffuse X-ray

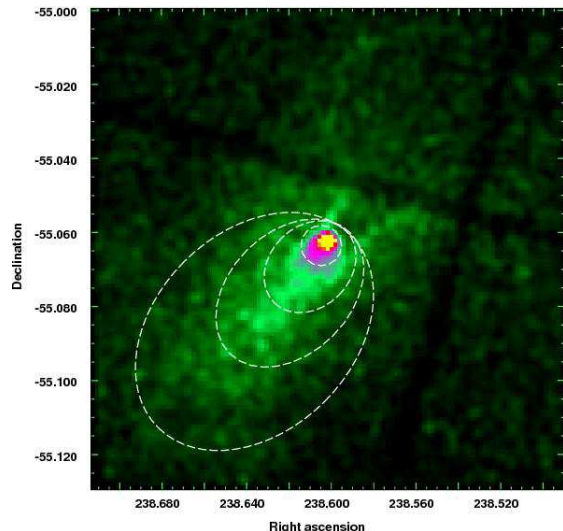


FIG. 3.— *Chandra* ACIS image of the inner region of G327.1-1.1 in the 0.5-10.0 keV energy band. The image was smoothed with a 2 pixel Gaussian function and shows a compact source, embedded in a cometary structure. The white dashed regions are apertures from which spectra were extracted for the *Chandra*-ACIS data (see Section 2.2).

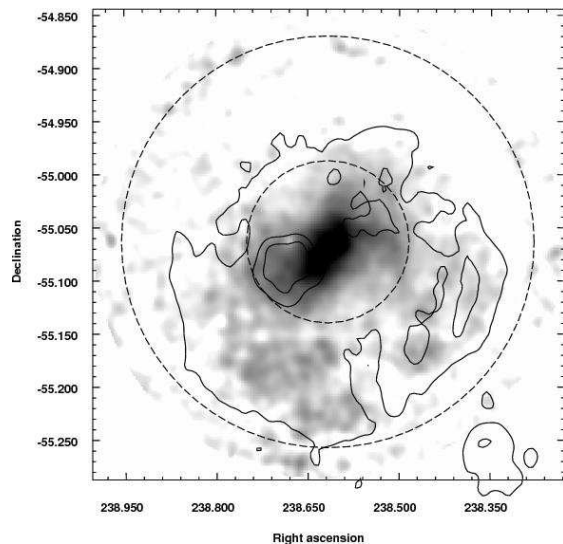


FIG. 4.— XMM-Newton combined MOS1 and MOS2 image of G327.1-1.1, in the 1.0-2.0 energy band, overlaid with the MOST radio contours. X-ray emission from almost the entire shell is detected in the XMM data and coincides well with the radio contours. The dashed circles in black are the spectral extraction regions for the XMM data (see Section 2.2).

emission elongated in the direction along the finger. The emission from the compact source does not have a profile of a point source, but is slightly extended and may consist of a point source imbedded in a more extended region. Figure 3 shows the detailed structure of this region. The image is binned by a factor of 8, smoothed with a 2 pixel Gaussian, and has not been exposure corrected. The compact source is embedded in a cometary structure from which an X-ray trail extends in the southeast direction. A pair of prong-like structures appears to originate from the vicinity of the compact source and extends out to the northwest. The most unusual feature in the X-ray images is a bubble-like structure that extends out from

the prongs. The bubble is approximately 3 arcminutes in diameter and can be seen in both *Chandra* and XMM images. The bubble is indicated by the black arrows in Figure 2a and is also evident in Figure 10, where the unsmoothed *Chandra* image is shown in blue/green and the radio image in red.

In the XMM MOS images, we detect the emission from nearly the entire radio shell. The combined MOS1 and MOS2 image in the 1.0-2.0 keV band, overlaid with the radio contours, is shown in Figure 4. The X-ray emission coincides well with the radio contours of the thermal shell. As in the radio image, the non-thermal component in X-rays is displaced from the geometric center of the X-ray shell.

3.2. Spectroscopy

In order to determine the general spectral properties of the X-ray emission in G327.1-1.1, spectra were extracted from two different regions in the XMM data, the inner PWN region and the outer shell. A circular aperture $5\frac{1}{2}$ in diameter, centered at 15:54:28.2, -55:03:49.25, was used for the PWN region, and an annulus with the same center coordinates and an inner and outer radii of $5\frac{1}{2}$ and $11\frac{1}{6}$ was used for the shell region (see Figure 4). The spectra were fit with the *Ciao* 3.4 *Sherpa* software and are shown in Figure 5. The spectra extracted from MOS1 and MOS2 data were fit simultaneously. The absorption column density, photon indices of the power law models, and temperatures of the thermal models were linked for the MOS1 and MOS2 fits, but the normalization parameters of each model were left to vary.

The spectrum extracted from the annular aperture and the best fit models are shown in the right panel of Figure 5. The emission appears to be thermal in nature and we see evidence of emission lines from NeX, MgXI, and SiXIII. Since we expect most of the emission in the annular aperture to be thermal emission from the shell, we attempted to fit the spectrum with a one component XSPEC Raymond & Smith thermal plasma model with fixed cosmic abundances. While a one component thermal model can account for most of the emission at lower energies, an additional component is needed in order to account for the excess emission at energies above 2 keV. Due to the high uncertainties in this region of the spectrum, this additional component can be fit equally well with a power law model with a photon index of 2.28 ± 0.16 , or a thermal model with a temperature of 3.3 ± 0.4 keV. While we cannot rule out the possibility that this residual high energy emission is non-thermal emission from the PWN particles that have diffused out to the outer remnant, in the fitting we assume that this emission is thermal emission from the background. In the final fit, we used a two component thermal model, which resulted in a 0.29 ± 0.01 keV temperature component that accounts for most of the total observed emission, and a 3.3 ± 0.4 keV temperature component, most likely due to residual Galactic background emission that was not accounted for by the blank sky background spectra. The summary of the best fit parameters for the shell region is listed in Table 1. The listed uncertainties are 90 % confidence, formal statistical uncertainties only.

While the spectrum of the inner PWN region of G327.1-1.1 is dominated by non-thermal emission with a power-law spectrum, it is obvious that an additional

TABLE 2
CHANDRA ACIS SPECTRAL FITTING RESULTS

PARAMETER	Region 1	Region 2	Region 3	Region 4
Area (arcsec ²)	1216	6124	15395	40105
Photon Index	1.65 ± 0.13	1.80 ± 0.13	2.03 ± 0.12	2.14 ± 0.14
F_X (total observed)(erg/cm ² /s)	7.8E-13	7.9E-13	9.1E-13	1.0E-12
F_X (unabsorbed non-thermal)(erg/cm ² /s)	1.4E-12	1.6E-12	2.2E-12	2.7E-12
F_X (unabsorbed thermal)(erg/cm ² /s)	...	2.1E-12	4.0E-12	1.5E-11
Reduced χ^2 Statistic	0.6	0.7	1.0	0.6

NOTE. — The extraction regions are shown in Figure 3. Listed uncertainties are 1.6 sigma (90 % confidence) statistical uncertainties from the fit. The spectra and fits are shown in Figure 6 and the fluxes were calculated in the 0.3-9.0 keV band.

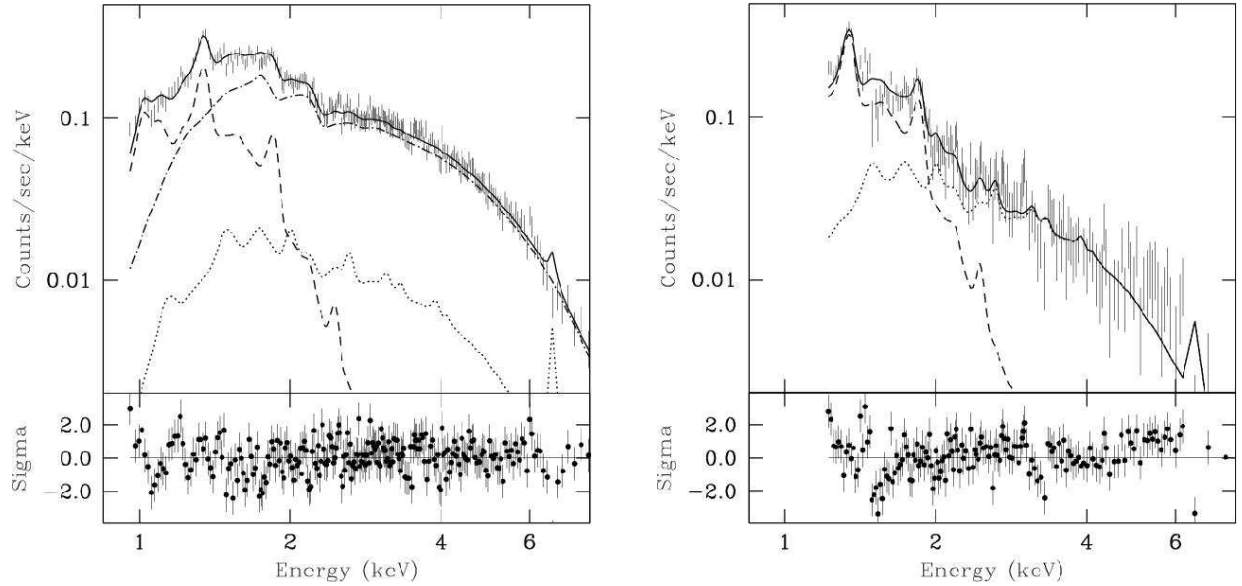


FIG. 5.— Spectra extracted from the XMM MOS1 data of the PWN region (left) and shell region (right). The solid lines represent the two component best fits to the spectra with the individual components shown as dotted and dashed curves. The PWN components are a power-law (dot-dashed curve), 0.3 keV thermal model (dashed curve), and the 3.3 keV thermal model attributed to the residual Galactic background (dotted curve). The shell components are a 0.3 keV thermal model (dashed curve) and the same 3.3 keV thermal residual background (dotted curve). The extraction apertures are shown as dashed circles in Figure 4. The PWN spectrum was extracted from the inner circle and the shell spectrum from the annulus defined by the two circles. The best fit parameters are listed in Table 1.

component is needed at energies below 2 keV. The spectrum was fit by an absorbed power law plus a thermal model, where the thermal model was the Raymond & Smith thermal plasma model with fixed cosmic abundances. The 3.3 keV thermal background component, found from the XMM spectral fitting of the shell region, was also added to the fit to account for the residual Galactic background. The temperature and normalization of the background component, scaled by the difference in extraction areas, were held fixed in the fit. Due to its small contribution, the fit parameters stay roughly the same even if this component is excluded from the fit. The left panel of Figure 5 shows the PWN spectrum and the best fit model. The power-law component is shown as the dot-dashed curve, the thermal component as the dashed curve, and the fixed thermal background as the dotted curve. The best fit power-law model has a photon index of 2.11 ± 0.03 and the thermal component has a temperature of 0.29 ± 0.01 keV. The parameters are summarized in Table 1.

In order to determine how the spectrum of the non-thermal emission varies with distance from the compact

source, spectra were extracted from the *Chandra* ACIS event files using four circular apertures shown in Figure 3, where each aperture excludes the counts from the enclosed apertures. For more details about background subtraction, refer to Section 2.2. Each of the spectra were fit with an absorbed power law plus a Raymond & Smith thermal plasma model whose temperature was fixed to 0.29 keV, as determined from the spectral fitting of the XMM-observed shell emission. The contribution from the residual 3.3 keV background component, found in the fitting of the XMM-observed shell emission, is negligible compared to the non-thermal emission inside the ACIS apertures and was not included in the fit. The value of N_H was fixed to $1.91\text{E}22\text{ cm}^{-2}$, the value found from the XMM data. The spectra and best fit models are shown in Figure 6 and the best fit parameters are summarized in Table 2. As expected, the emission across the PWN is dominated by non-thermal emission, but the spectrum extracted from the larger aperture clearly requires an additional thermal component at energies below 2 keV. The best fit values for the photon indices show that the spectrum is steepening with distance from the compact

source. This is consistent with the synchrotron burn-off of high energy electrons at larger distances from the compact source.

3.3. Timing Analysis

The *XMM* PN data in the small window mode (6 ms time resolution) was used to search for the pulsed signal from the compact source in G327.1-1.1. Events in the 0.5-10.0 keV and 2.0-7.0 keV bands were extracted from a circular aperture with a radius of $20''$, centered on 15:54:24.5, -55:03:45.1 (see Section 4.3.2). We used the Z_n^2 test (Bucccheri et al. 1983) with one harmonic to perform a timing analysis on a total of ~ 6900 events between 0.5-10 keV and ~ 4000 events between 2.0-7.0 keV, 50% of which can be attributed to the compact source, and the rest to the local background. In Section 4.3.2, we show that the spatial structure of the compact source in the *Chandra* data is composed of a point source embedded in a more extended structure that accounts for the majority the emission. When we fit the extended component with a Gaussian, the point source, assumed to be the pulsar, accounts for less than 10% of the total flux in the compact source. This makes it undetectable above the local background, even with pulsed fraction of 100 %. It may be possible that the point source contributes a larger fraction to the total flux, since the spatial profile of the underlying extended component is unknown. We searched for periodicity in the 1E-05 to 83 Hz frequency range, with a step size of 3E-06 Hz, a factor of 3 over-sampling compared to $1/T$, where T is the duration of the observation. We found no peaks with a probability below 10^{-3} , representing a 3 sigma confidence level.

4. DISCUSSION

4.1. Thermal Emission

XMM images of G327.1-1.1 reveal emission from the entire shell structure observed in the radio. Figure 4 shows the *XMM* image in the 1-2 keV band overlayed with the MOST radio contours, which coincide extremely well with the X-ray emission. Spectral fitting of the shell region indicates that the emission is thermal and well described by a 0.3 keV thermal plasma. We used the best fit temperature of the thermal shell to estimate the physical properties of the remnant based on the Sedov (1959) simple blast wave model, in which a supernova with the explosion energy of E_0 expands into an ISM with a uniform density, n_0 . We assume that the ISM is compressed into a shell with four times the initial ambient density, and a thickness of $1/12$ of the remnant radius, R . In our calculations, we also assume a complete shell, a remnant radius of $8'5$, as measured from the radio image, and equal ion and electron temperatures. The distance to G327.1-1.1 is not well determined and introduces the greatest uncertainty in the derived parameters. We adopt a distance of 9.0 kpc, which was estimated by Sun et al. (1999) based on the statistical relation between the hydrogen column density in the X-ray band and E(B-V) (Ryter et al. 1975), and the relation between E(B-V) and distance (Lucke 1978).

The following equations were used to calculate the remnant radius, R , shock velocity, v_s , and the ISM density, n_0 , where the last equation is based on the fitted intensity of the X-ray spectrum and the assumed geometry.

TABLE 3
INPUT AND DERIVED
PROPERTIES FOR THE
SEDOV MODEL

Property	Value
$D(kpc)$	9.0
$T(keV)$	0.3
$R(pc)$	22
$v(km/s)$	500
$t(yr)$	18000
$n_0(cm^{-3})$	0.12
$M(M_\odot)$	31
$E_{51}(10^{51}erg)$	0.5

NOTE. — A distance of 9.0 kpc was assumed in the calculations.

The equations are given as a function of the angular size of the remnant in arcminutes, R_{ang} , the distance in kiloparsecs, D_{kpc} , and the shell temperature, T_{keV} .

$$R(pc) = 0.291 R_{ang} D_{kpc} \quad (1)$$

$$v_s(km\ s^{-1}) = 928 T_{keV}^{1/2} \quad (2)$$

$$n_0(cm^{-3}) = 9.14 R_{ang}^{-3/2} D_{kpc}^{-1/2} \quad (3)$$

The Sedov (1959) model yields the following relations for the remnant age, t , SN explosion energy, E_0 , and the swept up mass, M .

$$t(yr) = 124 R_{ang} D_{kpc} T_{keV}^{-1/2} \quad (4)$$

$$E_0(10^{51}erg) = 2.87 \times 10^{-4} R_{ang}^{3/2} D_{kpc}^{5/2} T_{keV} \quad (5)$$

$$M(M_\odot) = 5.22 \times 10^{-3} R_{ang}^{3/2} D_{kpc}^{5/2} \quad (6)$$

The derived values for G327.1-1.1 are listed in Table 3 and appear to be reasonable for a remnant in the Sedov-Taylor stage. Since the model assumes a uniform ambient density, and a single average thermal temperature, the derived parameters have unquantifiable uncertainties due to uncertainties in the distance and the likely inhomogeneities in the ambient ISM that would cause variations in density and temperature across the shell.

4.2. Non-thermal Emission

The central part of G327.1-1.1 is dominated by a non-thermal X-ray component whose total emission can be described by a power-law model with a photon index of 2.08 ± 0.03 , typical for a PWN. The X-ray data provide evidence for the existence of a pulsar powering the PWN. Based on the empirical relationship between the pulsar's current spin-down energy loss rate and the luminosity of the non-thermal emission (Seward & Wang 1988), Sun et al. (1999) estimated a pulsar period (P) of 62 ms, period derivative (\dot{P}) of $8.9 \times 10^{-14} s\ s^{-1}$, and a surface magnetic field (B_0) of $2.3 \times 10^{12} G$. In this section, we follow the discussion by Sun et al. (1999) and

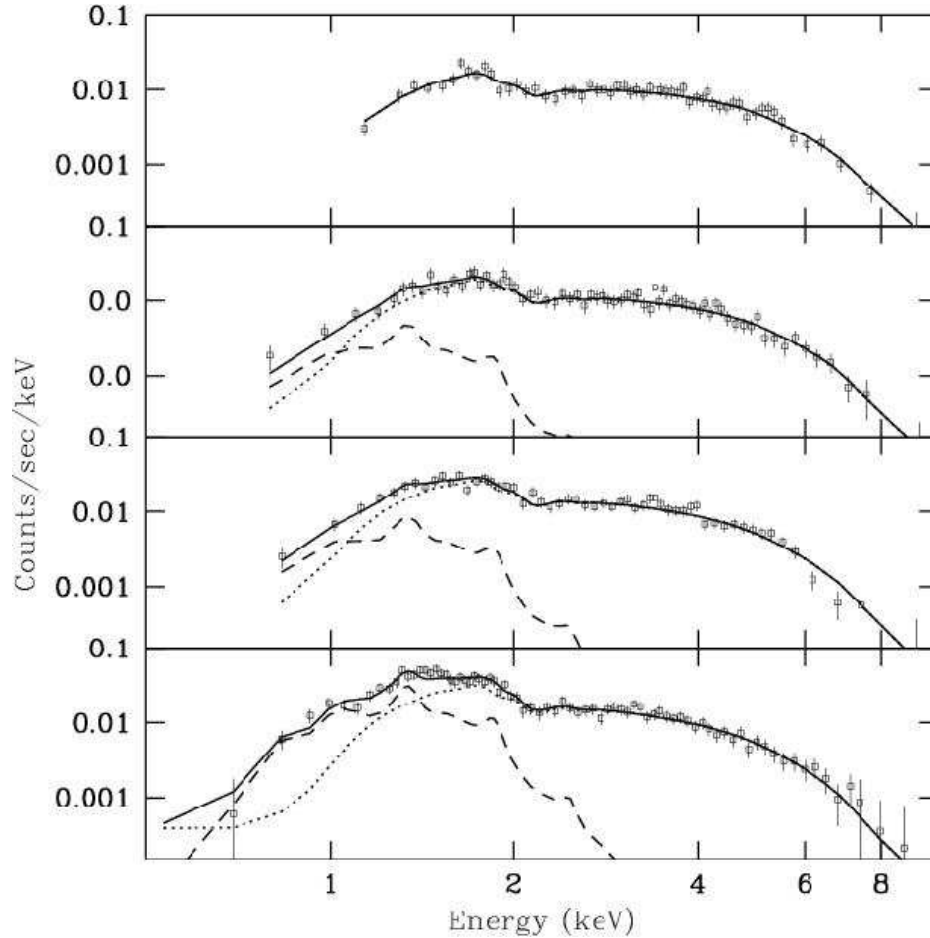


FIG. 6.— Spectra extracted from the *Chandra* ACIS data using the elliptical apertures shown in Figure 3. Each of the larger apertures excludes the counts from the inner ones and the spectral plots (top to bottom) are ordered by the aperture size (smallest to largest). The solid line represents the best fit two component model, power-law and thermal. The individual components are represented by dashed curves for the thermal component and dotted curves for the power-law component. The best fit parameters are listed in Table 2.

derive the same pulsar and PWN properties for comparison. We assume the same distance of 9.0 kpc and the remnant properties that we derived in Section 4.1 (Table 3).

The unabsorbed flux from the non-thermal component in the XMM data is $8.0 \times 10^{-12} \text{ erg cm}^{-2} \text{ s}^{-1}$ in the 2-10 keV band. Based on a more recent relationship between the pulsar’s spin-down energy loss rate and the non-thermal luminosity, $\log L_{X,(2-10\text{keV})} = 1.34 \log \dot{E} - 15.3$ (Possenti et al. 2002), and a distance of 9.0 kpc, this yields a spin-down energy, \dot{E} , of $2.8 \times 10^{37} \text{ erg s}^{-1}$. Using an SNR age of 18000 yr, we derive the following values; $P = 35 \text{ ms}$, $\dot{P} = 3.1 \times 10^{-14} \text{ ss}^{-1}$, and $B_0 = 1.0 \times 10^{12} \text{ G}$. Due to the very large uncertainties associated with the distance and age of G327.1-1.1, the calculated values are only rough approximations and are consistent with previous estimates by Sun et al. (1999).

4.3. Evolution and Morphology

The evolution of a PWN inside a composite SNR can be divided into three stages when the pulsar is not moving; the supersonic expansion stage, the reverse shock interaction stage, and the subsonic expansion stage. In the initial supersonic expansion stage, the PWN is bounded by a strong shock as it expands into the surrounding SN ejecta. The reverse shock eventually encoun-

ters the PWN surface and crushes the nebula, causing it to reverberate. After the reverse shock interaction stage, the PWN continues to expand subsonically into the SN ejecta that has been heated by the reverse shock (van der Swaluw et al. 2001; Blondin et al. 2001).

In the case where the pulsar is moving through the SNR at a high velocity, as it appears to be the case for G327.1-1.1, the evolution and morphology become much more complex. Initially, the PWN is carried along with the moving pulsar and the reverse shock first interacts with the PWN surface that is closest to the SNR shell. The PWN is swept away from the pulsar, resulting in a relic PWN that is located at a position opposite of the pulsar motion. After the passage of the reverse shock, the moving pulsar continues to generate a PWN that is now expanding subsonically into the reheated SN ejecta and is connected to the old, relic PWN. An additional stage of PWN evolution becomes evident when the pulsar’s velocity becomes supersonic and the head of its PWN deforms into a bow shock (van der Swaluw et al. 2004).

In the case of G327.1-1.1, we observe a bright radio PWN, which may be interpreted as the older, relic PWN, left behind after the passage of the reverse shock. van der Swaluw et al. (2004) gives an expression for the timescale, t_{col} , for the reverse shock to collide with the entire PWN surface,

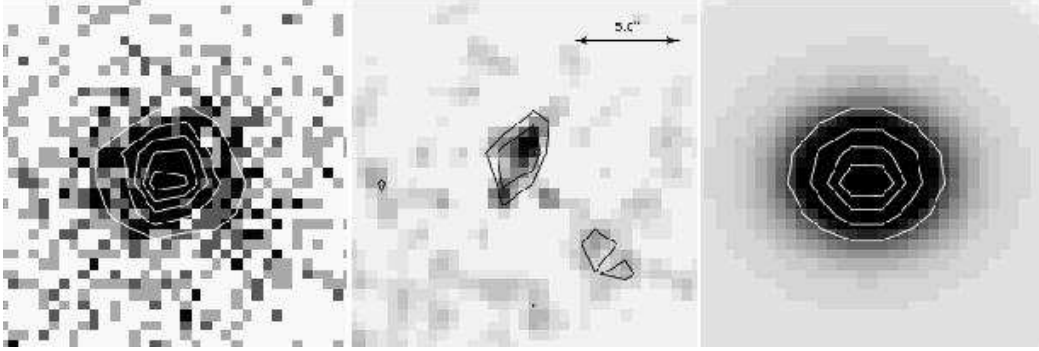


FIG. 7.— The left panel shows the unsmoothed *Chandra* image of the compact source region. The right panel is the image of the best fit model to the compact source emission, consisting of a point source and a more extended Gaussian component. The middle panel is the residual image. All three panels are displayed on the same linear scale from 0-16 counts.

$$t_{col} = 1045 E_{51}^{-1/2} \left(\frac{M_{ej}}{M_{\odot}} \right)^{5/6} n_0^{-1/3} \text{yr}, \quad (7)$$

where E_{51} is the explosion energy in units of 10^{51} erg , and M_{ej} is the ejected mass. Assuming an ejected mass of $10 M_{\odot}$, and using the derived values from Table 3, we find the timescale for the reverse shock collision to be on the same order as the derived SNR age of 18000 yr. This suggests that the PWN is either still in the reverse shock interaction stage, or that the reverberations from the collision between the reverse shock and the PWN have died out and the expansion of the overall PWN structure has become subsonic. The displacement of the relic PWN in G327.1-1.1 cannot be explained by the asymmetries due to the pulsar motion alone. Its displacement is not aligned with the X-ray trail or the radio finger, but is instead located further to the east. In order to explain the displacement of the PWN from the center of the SNR shell, a combination of the pulsar motion and an asymmetric reverse shock may be required.

Chandra observations clearly show that the compact source is surrounded by an extended, cometary structure, with an average radius of approximately half an arcminute (see Figures 2,3, and 8). According to hydrodynamic simulations of van der Swaluw et al. (2004), there are two possible scenarios that may give rise to this type of morphology. The pulsar may be moving at a supersonic velocity with respect to the SNR, causing the PWN to deform into a true bow shock, or the reverse shock has disrupted the PWN from the NW, giving rise to the cometary morphology.

4.3.1. Pulsar Velocity and Bow Shock Formation

The formation of the bow-shock is expected to occur at half the crossing time, t_{cr} (defined as the age of the remnant when the pulsar reaches the SNR shell), assuming that the remnant is in the Sedov-Taylor stage (van der Swaluw et al. 2003);

$$t_{cr} \simeq 1.4 \times 10^4 E_{51}^{1/3} V_{1000}^{-5/3} n_0^{-1/3} \text{yr}, \quad (8)$$

where V_{1000} is the pulsar velocity in units of 1000 km s^{-1} . At this time, the pulsar is positioned at a distance equal to two thirds of the blast wave radius, R (van der Swaluw et al. 2004). Using the physical parameters for G327.1-1.1, we find that the pulsar velocity would need to be $\sim 770 \text{ km s}^{-1}$ in order for the

TABLE 4
BEST-FIT PARAMETERS FOR THE
CHANDRA SPATIAL MODELING OF
THE COMPACT SOURCE IN G327.1-1.1

PARAMETER	Value
Delta Function	
Center coordinates	15:54:24.5, -55:03:45.1
Amplitude	$48 \pm 19 \text{ counts}$
Total flux	48 counts
Gaussian	
Center coordinates	15:54:24.4, -55:03:44.6
FWHM	$5''.5 \pm 0''.5$
Ellipticity	0.21 ± 0.08
Total flux	749 counts
Background level	
Amplitude	$1.1 \text{ counts arcsec}^{-2}$

current age of the remnant to be larger than half the crossing time t_{cr} . This is the pulsar velocity required for the bow-shock formation to have already taken place in G327.1-1.1. The approximate displacement of the compact source in G327.1-1.1 from the geometric center of its radio shell is 7.5 parsecs. This is also the approximate length of the radio finger, which is presumably the pulsar trail. Using this projected distance and the derived age, we calculate the tangential pulsar velocity to be on the order of $\sim 400 \text{ km s}^{-1}$. This would require a 30 degree angle between the pulsar velocity and the line of sight to achieve a velocity of 770 km s^{-1} , required for bow-shock formation. While the required pulsar velocity is somewhat high for a typical pulsar, it is not entirely unreasonable and cannot discount the possibility that the structure in Figure 3 is the head of the PWN that has already been deformed into a bow shock.

4.3.2. Spatial Modeling of the Compact Source

At the tip of the radio finger, the *Chandra* image shows a compact source whose spatial profile is significantly more extended than that of a point source (see Figure 2b). Figure 9 shows the contours and scales for the three main emission regions in the *Chandra* image, the compact source region in the innermost contour, the cometary region in the middle contour, and the elongated X-ray emission that is coincident with the radio finger in

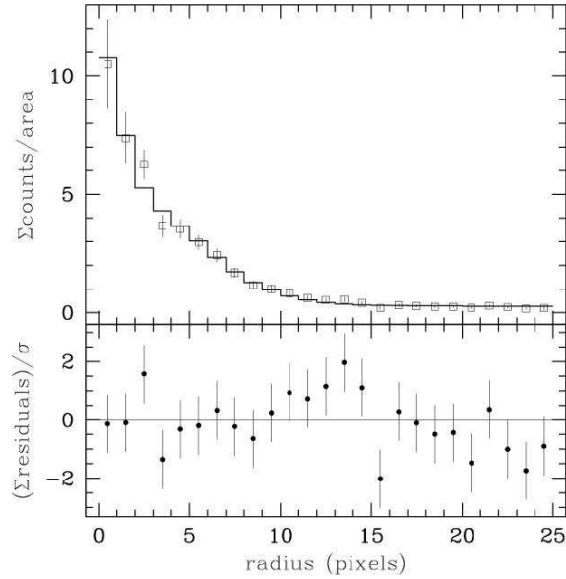


FIG. 8.— *Chandra* emission profile of the compact source region. The curve representing the best fit model composed of a *Chandra* PSF and a more extended Gaussian component. The profile is centered at the coordinates 15:54:24.5, -55:03:45.1, and each pixel corresponds to a spatial size of $0''.5$.

the outer contour. We used Sherpa to spatially fit the unbinned image of the compact source region in the 0.3 to 9.0 keV energy band. The fitting was performed on a circular section of the image, 24 pixels ($\sim 12''$) in radius, centered on the brightest region of the compact source. A normalized image of a 3 keV point spread function, generated with the Ciao tool *mkpsf*, was used as a convolution kernel in the fitting. We used a model consisting of a delta function plus a Gaussian, and a level offset for the local background surrounding the compact source. The spatial profile and the best fit model are shown in Figure 8a. The best fit model consists of a delta function with an amplitude of 48 ± 19 counts, a Gaussian with a fwhm of $5''.5 \pm 0''.5$, and an ellipticity of 0.21 ± 0.08 , and a background offset of 1.1 counts arcsec $^{-2}$. The quoted uncertainties represent 1-sigma errors on the fitted parameters. The center coordinates of the delta function and the Gaussian components are 15:54:24.5, -55:03:45.1, and 15:54:24.4, -55:03:44.6, respectively. The total fluxes inside the $12''$ radius aperture are 48 counts in the point source component and 749 counts in the extended, Gaussian component. The best-fit values are summarized in Table 4. Figure 7 shows the *Chandra* image of the compact source region in the left panel, the image of the best fit model in the right panel, and the residual image in the middle panel. We note that the residual image shows a slightly elongated knot of emission, approximately $4''$ in length, that originates near the peak of the point source and extends to the northwest. The residual emission in the brightest pixels of the knot is approximately 5 sigma above the noise.

The results of the fitting suggest that the emission originates from a point source, assumed to be the pulsar, embedded in a more extended structure which accounts for 94 % of the compact source flux. A similar type of emission was seen in the Mouse (Gaensler et al. 2004) bow shock nebula, where the X-ray emission from its compact source is also composed of a point source embedded

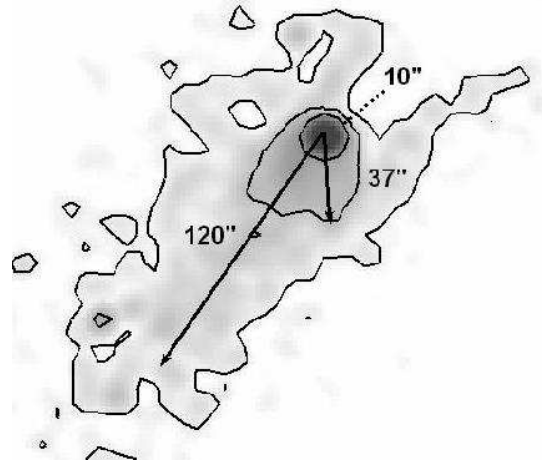


FIG. 9.— The contours and spatial scales for the three main emission regions in the *Chandra* image; the compact source region inside the innermost contour, cometary structure inside the middle contour, and the extended X-ray emission inside the outermost contour.

in a broader component, $2''.4$ in size. In the Mouse, this emission is contained within the termination shock of the pulsar and it was attributed to X-ray knots that are produced in its vicinity (Gaensler et al. 2004). In the case of G327.1-1.1, the size of the extended component is much broader, $\sim 12''$ in diameter, and the emission is surprisingly uniform. A possible explanation for the origin of this emission is the shocked pulsar wind downstream of the termination shock, which would require the boundary of the shock to be on a much smaller scale than the spatial extent of the compact source and well within the innermost contour of Figure 9.

4.3.3. Prong and Bubble Structures

The most unusual feature in the *Chandra* and XMM images are two prong-like structures that extend into a faint bubble, approximately 3 arcminutes in diameter (Figures 2 and 3). The prongs are approximately 1.5 arcminutes in length and their axes are not aligned with the position of the compact source, which is presumably the pulsar. It seems unlikely that the prongs and bubble structures are from the SNR itself and that their position only coincidentally falls along the line of sight to the position of the pulsar and is aligned along the direction of the pulsar motion. The structures may arise from the violent interaction between the reverse shock and the PWN that would cause the pulsar wind material to mix in with the SNR ejecta.

4.3.4. Size of the PWN and Pulsar Wind Cavity

In this section, we estimate the expected sizes of the PWN and the pulsar wind cavity for two scenarios and compare them to the observations; the case where the PWN has reformed and is now expanding subsonically, and the case where the PWN has been deformed into a bow shock, due to the pulsar motion. In Section 4.2 we found that the timescale for the reverse shock to interact with the entire PWN surface of G327.1-1.1 is on the same order as the remnant age. We note that the uncertainty on these estimates is high and that it is possible that the PWN has entered the subsonic stage of expansion. Here we assume that the PWN is expanding subsonically, and

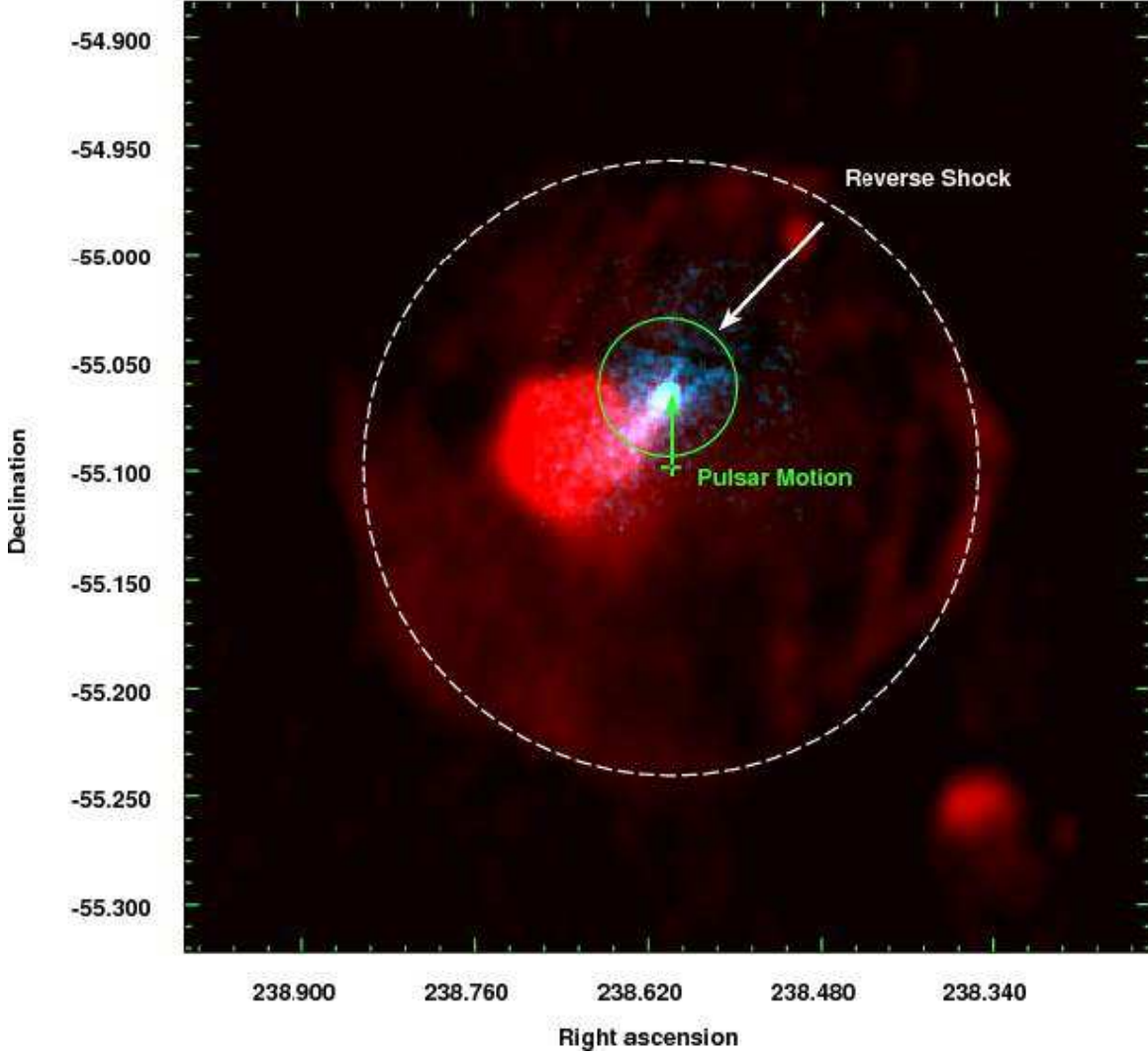


FIG. 10.— The MOST radio image is shown in red and Chandra ACIS X-ray image in blue/green. The figure illustrates a possible physical scenario that could give rise to the observed radio and X-ray morphology. The white dashed circle is the boundary of the radio shell, the green cross is the geometric center of the shell, the green arrow represents a possible direction of the pulsar motion, the green circle is the position of the PWN immediately before the passage of the reverse shock, and the white arrow indicates the proposed direction of the reverse shock.

has reached a pressure equilibrium with the SNR, after the passage of the reverse shock, in order to make rough estimates of the relative sizes of the SNR radius, (R_{SNR}), the PWN radius (R_{PWN}), and the termination shock radius (R_{ts}). Following van der Swaluw et al. (2001) and setting P_{pwn} equal to P_{snr} , the radius of the PWN can be expressed as

$$R_{PWN} \simeq \left(\frac{\dot{E}t}{E_0} \right)^{1/3} R_{SNR}, \quad (9)$$

where \dot{E} is the mechanical luminosity driving the pulsar wind, found in Section 4.2, and t is the time passed since the passage of the reverse shock (t_{SNR} minus t_{col}). In Section 4.3, we calculated that t_{SNR} and t_{col} are on the same order of magnitude, but the values are associated with very large uncertainties. For the purpose of our calculation, we set t equal to 5000 yr. Setting the pressure of the relativistic wind terminated at a radius R_{ts} (Kennel & Coroniti 1984) equal to the SNR pressure, we

obtain the following expression for R_{ts}

$$R_{ts} \simeq \sqrt{\frac{\dot{E}}{cE}} R_{snr}^{3/2}. \quad (10)$$

Using the parameters for G327.1-1.1, and our estimate of \dot{E} from Section 4.2, we estimate that $R_{PWN} \simeq 2.7 pc t_{1000 yr}^{1/3}$, or $\sim 60'' t_{1000 yr}^{-1/3}$. Since the average extent of the X-ray emission observed by *Chandra* is on the order of $60''$ (see Figure 9), the time since the reverse shock collided with the PWN should be $\sim 1000 yr$. The prongs and bubble structures ahead of the pulsar may be caused by the turbulent interaction between the reverse shock and the PWN, and may provide further evidence for a somewhat recent reverse shock collision. We calculate a termination shock radius of $0.25 pc$, or $6''$, roughly the same size as the extent of the compact source seen in the *Chandra* image (indicated by the innermost contour of Figure 9). Even though the estimated values are only first order estimates, the predicted size of R_{ts} indicates

that the pulsar wind cavity is too small to be associated with the observed cometary structure. In this scenario, the cometary morphology may be caused by the passage of the reverse shock, which disrupted the reformed PWN from the NW direction.

As an alternative, we consider the case in which the PWN has been deformed into a bow shock and make similar estimates to compare with our observations. We assume a pulsar velocity of 770 km/s, the minimum required velocity for bow shock formation, found in Section 4.3.1. Following the discussion by van der Swaluw et al. (2003), we calculate the values of the pressure behind the SNR blast wave, P_{sh} , pulsar mach number, M_{psr} , bow shock pressure, P_{bs} , leading to the the radius of the forward termination shock, R_{ts}^F (equations 6, 10, 16, and 21 of van der Swaluw et al. (2003)). Using the parameters for G327.1-1.1 and γ of 5/3, we calculate that $P_{sh} = 5.2 \times 10^{-10} \text{ dyne cm}^{-2}$, $M_{psr} = 2.8$, $P_{bs} = 4.7 \times 10^{-9} \text{ dyne cm}^{-2}$, and finally $R_{ts}^F = 0.033 \text{ pc}$, or $0''.8$, based on a distance of 9.0 kpc. The radius of the backward termination shock would then be on the order of $2''.7$, making the entire extent of the termination shock $\sim 3''.5$ (Bucciantini 2002; van der Swaluw et al. 2003). This is somewhat smaller, but on the same order of magnitude as the size of the compact source in G327.1-1.1. The expected size of the contact discontinuity radius is $\approx 1.33 R_{ts}^F = 0.04 \text{ pc}$, or $1''$ (Bucciantini 2002; van der Swaluw et al. 2003; Gaensler et al. 2004). Based on these estimates, the cometary structure in the *Chandra* image appears too large to be attributed to the contact discontinuity, since it extends at least $8''$ beyond the extent of the compact source in the forward direction (see Figure 9). The relative sizes of the observed structures are not consistent with estimated sizes from bow shock simulations, but due to the large uncertainties in the derived parameters for G327.1-1.1, we cannot rule out the bow shock scenario on this basis alone. However, we note that the observed X-ray emission ahead of the pulsar in the form of prongs and bubble structures, does suggest that the cometary structure that we are observing is most likely not a bow shock.

4.3.5. Possible Physical Scenario

There are two possible scenarios that may give rise to the cometary morphology observed in G327.1-1.1; the newly forming PWN may be deformed into a bow shock when the pulsar velocity becomes supersonic, or an asymmetric passage of the reverse shock may disrupt the PWN from one side and give rise to the cometary morphology. While we were not able to rule out either scenario, the latter appears to be a more likely based on the observed X-ray emission ahead of the pulsar (see Section 4.3.4). We suggest that PWN in G327.1-1.1 is in the subsonic stage of expansion, after the passage of the reverse shock. Figure 10 illustrates a possible physical scenario that could explain the observed morphology. If we assume that the pulsar was born in the geometric center of the radio shell, indicated by a white dashed circle, its current position suggests that the velocity vector is in the north direction, as indicated by the green arrow. Before the passage of the reverse shock, the PWN was expanding supersonically and was being carried along with the

moving pulsar to the north. The position of the PWN immediately before the passage of the reverse shock would therefore be north of the remnant center, as shown by the green circle in Figure 10. If inhomogeneities in the ISM caused the reverse shock to reach the PWN from the NW direction first, it would displace the PWN to the location of the radio relic and cause the newly forming PWN to take on the observed cometary morphology (van der Swaluw et al. 2004). Hydrodynamic simulations of van der Swaluw et al. (2004) show the various stages of this process, with the main difference being that an additional asymmetry, besides the pulsar’s velocity vector, is required to explain the morphology. In order for the reverse shock to first reach the PWN surface from the northwest direction, a higher ISM density in the West would be required, which cannot be confirmed or ruled out by our data.

5. CONCLUSIONS

In this paper, we analyzed the *Chandra* and *XMM* imaging and spectroscopy of G327.1-1.1 in order to characterize the nature of the X-ray emission, determine the properties of the SNR and the pulsar progenitor, and understand the evolutionary and physical scenario that would lead to the observed morphology. The X-ray images show an extended compact source that is embedded in a cometary structure, from which a trail of emission extends towards the bright radio PWN. Prong-like structures originate near the compact source and extend into a faint bubble, 3 arcminutes in diameter. A symmetric shell coincident with the shell observed in the radio is evident in the 1-2 keV *XMM* image. The X-ray spectrum of the PWN is described by a power-law model with an average photon index of 2.11 ± 0.03 . The shell emission is best described by thermal model with a temperature of $0.30 \pm 0.01 \text{ keV}$. Using the Sedov model and assuming a distance of 9 kpc, we calculate a remnant radius of 22 pc, an age of 18000 years, shock velocity of 500 km/s, n_0 of 0.12 cm^{-3} , a swept-up mass of $31 M_{sol}$, and an explosion energy of $0.5 \times 10^{51} \text{ ergs}$. Since the remnant has most likely expanded into a nonuniform medium, the derived dynamical properties are expected to vary.

Based on the timescale for reverse shock interaction and the derived remnant age, it is possible that G327.1-1.1 is in the subsonic expansion stage of its evolution. While we can not discount the possibility of a bow shock formation in G327.1-1.1 based on the calculations of the relative sizes of the PWN and the termination shock radii, the observed X-ray emission ahead of the pulsar makes the bow shock scenario less likely. The cometary morphology may be explained by the passage of the reverse shock from the northwest direction that disrupted the newly forming PWN, which was originally located north of the SNR center.

Support for this work is provided by NASA Grant GO6-7053X. B.M.G. acknowledges support from the Australian Research Council through a Federation Fellowship (grant FF0561298). P.O.S. acknowledges support from NASA contract NAS8-03060.

REFERENCES

- Blondin, J. M., Chevalier, R. A., & Frierson, D. M. 2001, *ApJ*, 563, 806
- Blondin, J. M., Wright, E. B., Borkowski, K. J., & Reynolds, S. P. 1998, *ApJ*, 500, 342
- Bochinno, F. & Bandiera, R. 2003, *A&A*, 398, 195
- Buccheri, R., et al. 1983, *A&A*, 128, 245
- Bucciantini, N. 2002, *A&A*, 387, 1066
- Carter, J. A., & Read, A. M. 2007, *A&A*, 464, 1155
- Clark, D. H., Caswell, J. L., & Green, A. J. 1973, *Nature*, 246, 28
- Clark, D. H., Caswell, J. L., & Green, A. J. 1975, *Australian Journal of Physics Astrophysical Supplement*, 1
- Gaensler, B. M., van der Swaluw, E., Camilo, F., Kaspi, V. M., Baganoff, F. K., Yusef-Zadeh, F., & Manchester, R. N. 2004, *ApJ*, 616, 383
- Gaensler, B. M., Chatterjee, S., Slane, P. O., van der Swaluw, E., Camilo, F., & Hughes, J. P. 2006, *ApJ*, 648, 1037
- Kennel, C. F., & Coroniti, F. V. 1984, *ApJ*, 283, 710
- Lamb, R. C., & Markert, T. H. 1981, *ApJ*, 244, 94
- Lucke, P. B. 1978, *A&A*, 64, 367
- Possenti, A., Cerutti, R., Colpi, M., & Mereghetti, S. 2002, *A&A*, 387, 993
- Ryter, C., Cesarsky, C. J., & Audouze, J. 1975, *ApJ*, 198, 103
- Sedov, L. I. 1959, *Similarity and Dimensional Methods in Mechanics*, New York: Academic Press, 1959
- Slane, P. et al. 1998, *Memorie della Societa Astronomica Italiana*, 69, 945
- Seward, F. D., & Wang, Z.-R. 1988, *ApJ*, 332, 199
- Seward, F. D., Kearns, K. E., & Rhode, K. L. 1996, *ApJ*, 471, 887
- Sun, M., Wang, Z., & Chen, Y. 1999, *ApJ*, 511, 274
- van der Swaluw, E., Achterberg, A., Gallant, Y. A., & Tóth, G. 2001, *A&A*, 380, 309
- van der Swaluw, E., Achterberg, A., Gallant, Y. A., Downes, T. P., & Keppens, R. 2003, *A&A*, 397, 913
- van der Swaluw, E., Downes, T. P., & Keegan, R. 2004, *A&A*, 420, 937
- Whiteoak, J. B. Z., & Green, A. J. 1996, *A&AS*, 118, 329